MDPI

Article

Failure Mechanism of EB-PVD Thermal Barrier Coatings under the Synergistic Effect of Thermal Shock and CMAS Corrosion

Xiaopeng Hu [1,2,†], Guolin Liu [1,2,†], Qing Liu [1,2], Wang Zhu [1,2,*], Sai Liu [1,2] and Zengsheng Ma [1,2]

1 Key Laboratory of Key Film Materials & Application for Equipment, School of Materials Science and Engineering, Xiangtan University, Xiangtan 411105, China
2 Key Laboratory of Low Dimensional Materials and Application Technology of Ministry of Education, School of Materials Science and Engineering, Xiangtan University, Xiangtan 411105, China
* Correspondence: wzhu@xtu.edu.cn
† These authors contributed equally to this work.

Abstract: Thermal barrier coatings (TBCs) suffer from the thermo-chemo-mechanical coupling action of thermal shock and calcium–magnesium–alumina–silicate (CMAS) corrosion. However, the failure mechanism of TBCs under the synergistic effect of thermal shock and CMAS corrosion is still unclear due to a lack of an environmental simulator. Herein, an 8YSZ ceramic coating is deposited on a PtAl bond coating/DD419 nickel-based single crystal superalloy substrate using the electron beam physical vapor deposition (EB-PVD) method. The thermo-chemo-mechanical coupling effect of TBCs is achieved in a self-developed environmental simulator. The interaction of volume expansion induced by the phase transition of ZrO_2, structural degradation and thermal fatigue further increases the out-of-plane tensile stress and in-plane shear stress in the ceramic coating, which accelerates the initiation and propagation of surface vertical cracks and horizontal cracks. As multiple surface vertical cracks propagate to the interface and merge with interfacial cracks, the ceramic coating spalls from the substrate.

Keywords: electron beam physical vapor deposition (EB-PVD); thermal shock; CMAS corrosion; thermo-chemo-mechanical coupling; failure mechanism

1. Introduction

Thermal barrier coatings (TBCs) are widely applied to gas turbine engines due to their excellent mechanical properties, high temperature resistance, low thermal conductivity and excellent thermal cycling performance [1–3]. TBCs can reduce the temperature of hot components and effectively improve the thrust–weight ratio and performance of aeroengines [4,5]. The coating 7~8 wt% yttria-stabilized zirconia (8YSZ) is widely used as a top ceramic coating in TBCs. There are two common methods to prepare the top ceramic coating: electron beam physical vapor deposition (EB-PVD) and plasma spraying (PS). EB-PVD TBCs are typically columnar crystal structures with good strain tolerance and damage resistance at high temperatures [6–8]. However, turbine blades are subjected to high-temperature oxidation, particle erosion and calcium–magnesium–alumina–silicate (CMAS) corrosion during the service. CMAS corrosion has become the most dangerous factor leading to coating failure [9–11]. As the service temperature increases, the siliceous minerals (dust, sand and volcanic ash) ingest the air deposit on the surface of hot-section components, resulting in glassy CMAS melts when the surface temperature exceeds 1200 °C. CMAS penetrates the 8YSZ coating, destroying the structural and chemical integrity of TBCs [12]. Furthermore, TBCs are subjected to the thermo-chemo-mechanical coupling action of thermal shock and CMAS corrosion. Therefore, it is urgent to investigate the failure mechanism of TBCs under the synergistic effect of thermal shock and CMAS corrosion.

Considerable work has been conducted to study the failure mechanism of TBCs. 8YSZ TBCs prepared using EB-PVD generate thermally grown oxide (TGO) during thermal

cycling tests, and the thermal mismatch induces tensile stress, which, in turn, promotes the occurrence of cracks, resulting in the failure of the coating at the interface [13,14]. In addition, EB-PVD TBCs exhibit a complex failure mechanism in a corrosive environment. The surface Zr^{4+} competes with Ca^{2+} for octahedral-coordinated garnet sites [15], and the molten CMAS infiltrates the middle area of the coating and fills the internal voids. The molten CMAS in the coating begins to solidify and increases the density of the whole coating, which causes changes in the thermal–mechanical properties of TBCs, such as elastic modulus [16,17]. The dissolution of Y_2O_3 in CMAS leads to the phase transition of t-ZrO_2 to m-ZrO_2 in the coating, and the mismatch stress caused by the volume difference of this phase transition accelerates the failure of TBCs during the cooling process [17,18]. Meanwhile, the CMAS reaches the bond's surface coating, leading to the formation of anorthite [19]. These factors lead to structural degradation of the coating and coating spallation. However, most of these experiments are in a constant temperature muffle furnace, which may affect the actual service performance [20]. TBCs are subjected to high temperature, flame impact and CMAS corrosion in the actual service environment. A huge difference exists between the actual service environment and a constant-temperature furnace condition [21]. A series of environmental simulators are being developed to approach the actual service environment. Laser beam and gas burners have been used as heating sources [22–26] to simulate the high-temperature stage, but they are far from reaching the harsh environmental conditions of TBCs. Furthermore, previous research focused on thermal shock or high-temperature CMAS corrosion. The synergistic effect of thermal shock and CMAS corrosion on TBCs is still lacking.

In this paper, an 8YSZ ceramic coating was deposited on a PtAl bond coating/DD419 nickel-based single-crystal superalloy substrate using the EB-PVD method. The thermo-chemo-mechanical coupling effect of TBCs was achieved in a self-developed environmental simulator. The failure mechanism of TBCs under the synergistic effect of thermal shock and CMAS corrosion was investigated.

2. Experimental Procedure

2.1. TBC Preparation

During the preparation of the TBC specimens, a nickel-based single-crystal superalloy (DD419) with a diameter of 30 mm and a thickness of 6 mm was selected as the substrate. The specific composition is shown in Table 1. The single-phase β-(Ni,Pt)Al coating was used as a bond coating. The preparation of the β-(Ni,Pt)Al coating included three steps [27]: Pt electroplating of the substrate, vacuum annealing and vapor-aluminizing treatment. Before depositing the bond coating, the substrate was ground with SiC papers and humidly grit-blasted with alumina (220# mesh) under 0.3 MPa. It was then degreased in boiling NaOH aqueous solution of 50 g/L for 10 min and ultrasonically cleaned in acetone and ethanol for 10 min each. Afterwards, the Pt plating was deposited in an alkaline Pt-plating solution at 80 °C with an effective Pt concentration of 6 g/L. The chemical composition of the Pt electroplating solution is given in Table 2. The plating current density was 9 mA/cm^2, and the deposition rate was about 3 μm/h. A deposited Pt plating with a thickness of 5 μm was obtained. Prior to aluminization, vacuum annealing was conducted at 1040 °C for 1 h to eliminate the residual stress and dilute the Pt content on the surface. High-pressure gas aluminizing treatment was conducted in a gaseous aluminizing furnace at 1070 °C for 5 h. The heating rate was kept below 8 °C/min. Detailed information on the preparation process of a single-phase β-(Ni,Pt)Al coating is described in the literature [27]. An 8YSZ ceramic coating with a thickness of 250 μm was deposited on the bond coating using the EB-PVD method. The detailed preparation parameters are shown in Table 3. A commercial 8YSZ ceramic target was used in the EB-PVD process. Before depositing the ceramic coating, the base material was annealed under a vacuum at 870 °C for three hours. To preheat the 8YSZ ceramic target, the preheating current and time were set as 0.01~0.1 A and 1~15 min, respectively. After preheating, the operating current was increased to 0.1~1 A. The average thickness of the ceramic coating was 250 μm, and the deposition rate was 3.5 μm/min.

Table 1. Normal chemical composition (wt.%) of single-crystal superalloy DD419.

Co	Ta	Cr	W	Mo	Re	Al	Ni
7.5	6.5	7	5	1.5	3	6.2	Bal.

Table 2. Chemical composition of the alkaline Pt-plating solution.

Composition	$Pt(NH_3)_2(NO_2)_2$	$Na(NO_2)$	$Na_3C_6H_5O_7 \cdot 2H_2O$	$CH_3COONa \cdot 3H_2O$	pH
Value	10 g/L	10 g/L	12 g/L	6 g/L	9

Table 3. Preparation parameters of EB-PVD for 8YSZ ceramic coating.

Layers	Current of Electron Beam (A)	Rotation Speed (rpm)	Voltage (KV)	Heating Temperature (°C)	Pressure in the Vacuum Chamber (Pa)
Ceramic coating	0.1~1.0	20	10	900 ± 50	133.32×10^{-5}

According to the sediment collected from the actual engine parts, the CMAS powder synthesized in the laboratory had a chemical composition of 33 mol% CaO, 9 mol% MgO, 13 mol% Al_2O_3 and 45 mol% SiO_2. Four kinds of oxides were mixed and ground in a ball mill for 8 h. Alcohol was added during ball milling to ensure uniform mixing before the mixed slurry was dried in an oven at 80 °C. The dried powder was calcined in a high-temperature muffle furnace at 1500 °C for 2 h to alter it to a molten state and then quenched in distilled water quickly. Finally, the CMAS powder was obtained with grinding and sieving (500# mesh).

2.2. Environmental Simulator of TBCs and Determination of Infrared Emissivity

The synergistic effect of thermal shock and CMAS corrosion on TBC performance was investigated in our developed environmental simulator, as shown in Figure 1. Aviation kerosene was used as fuel, and nitrogen was used to provide sufficient pressure for kerosene. Pure oxygen was used as a combustion improver to assist the full combustion of kerosene. A Laval nozzle was developed to produce the supersonic flame. The surface temperature of the TBC was monitored using an infrared thermometer.

Using a KT15II (Heitronics, Wiesbaden, Germany), the temperature was automatically controlled during the experiment by adjusting the distance between the supersonic flame-spraying gun and the specimen. An infrared thermal imager (GF309, Teledyne FLIR, Wilsonville, OR, USA) was used to obtain the temperature distribution of the TBC surface [28]. The substrate surface was cooled by the compressed air, which allowed the temperature gradient on the specimen's surface to be realized. The substrate temperature was measured using thermocouples during a thermal shock test. In order to reduce the randomness and error in the experiment, three 8YSZ coating specimens were used to repeat the experiment.

To ensure the temperature accuracy of non-contact infrared temperature measurement, the evolution of emissivity with temperature was determined. An illustration of the determination of infrared emissivity is shown in Figure 2. The determination of infrared emissivity is related to the distance and angle between the laser source and the specimen [29]. Figure 2 shows a movable calibrated emissivity device, which can determine the evolution of emissivity with temperature at different distances and angles. During the thermal shock test, the angle between the infrared thermometer and the specimen surface was 30°. A specimen was put in a high-temperature muffle furnace, and the furnace was heated to a specified temperature. Two thermocouples were placed on both sides of the specimen to measure the temperature. When the temperature difference between the two thermocouples was less than 3 °C, the temperature was kept for 30 min to ensure the isothermal condition. The infrared thermal imager was used to measure the surface temperature of the TBC. The emissivity was changed until the temperature corresponded to that of

the thermocouple. The emissivity at the corresponding temperature was then determined. The angle was fixed at 30°, and the distance between the infrared thermometer and the specimen was changed to obtain the emissivity at different distances. The emissivity data are given in Table 4. When the test temperature was 1250 °C and the distance was 53 cm, the emissivity was determined to be 0.963.
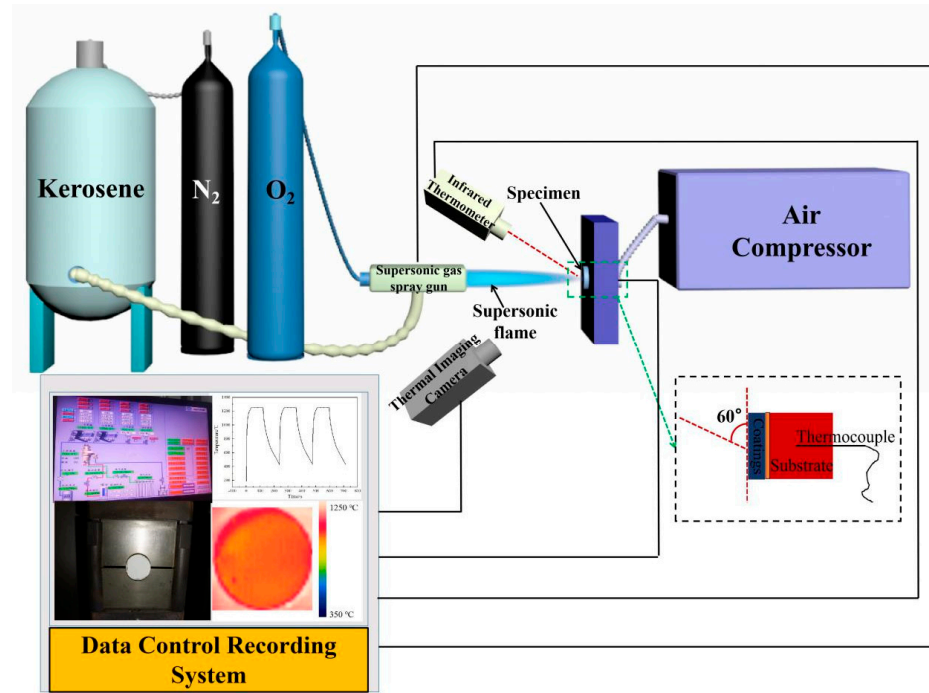

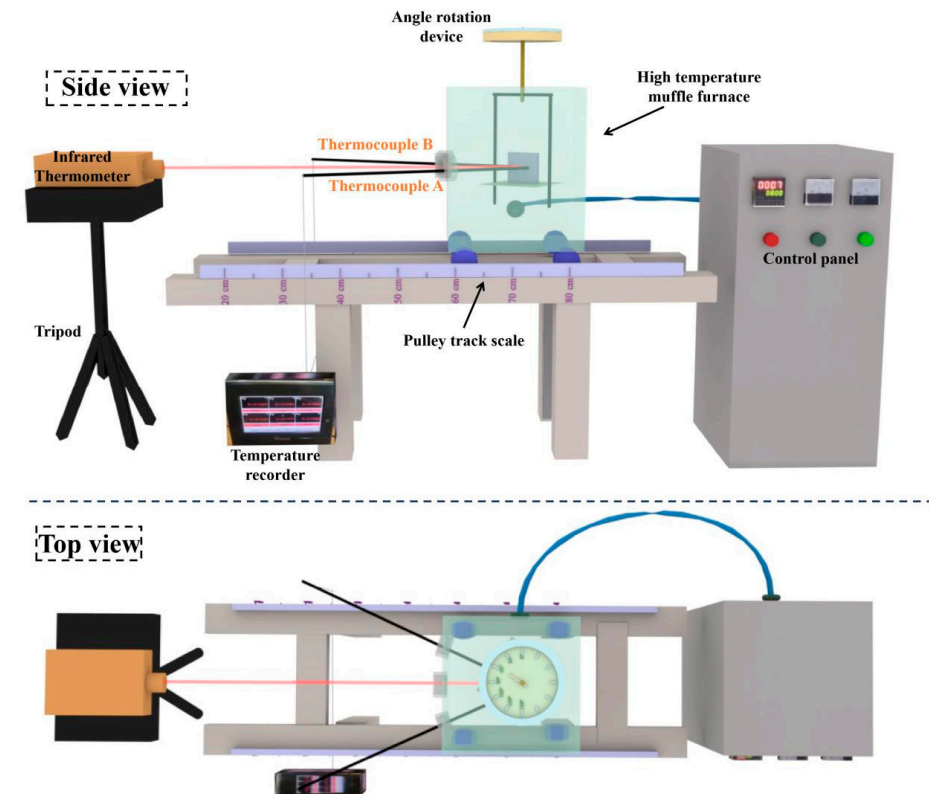**Figure 1.** Schematic diagram of the environmental simulator test system.

Figure 2. Schematic diagram of determination of emissivity.

Table 4. Evolution of emissivity of the 8YSZ ceramic coating with temperature.

Temperature Distance	1000 °C	1100 °C	1200 °C	1250 °C
70 cm	0.981	0.978	0.976	0.975
60 cm	0.982	0.976	0.975	0.973
53 cm	0.978	0.971	0.968	0.963

2.3. High-Temperature Experiment of TBCs under the Synergistic Effect of Thermal Shock and CMAS Corrosion

The CMAS powder and alcohol were evenly mixed to a viscous liquid paste and then uniformly coated on the surface of the TBC specimen and dried in a drying oven for 24 h. The CMAS concentration coated on the TBC surface was 10 mg/cm^2. The specimen was heated in a high-temperature furnace at 950 °C for 0.5 h, ensuring that the CMAS was sintered onto the TBC surface. The specimen coated with CMAS was put in the fixture. The thermal shock cycle is composed of heating, holding and cooling stages. As shown in Figure 3, the surface temperature of the TBC was heated from room temperature to 1250 °C in 30 s, held at 1250 °C for 90 s and then cooled to 400 °C in 120 s. The experimental parameters of the environmental simulator were tested to meet the requirement of the thermal shock cycle. The detailed experimental parameters of the environmental simulator are shown in Table 5. The specimen was cooled to room temperature, and 10 mg/cm^2 of CMAS coated the TBC surface every ten thermal shock cycles. It is worth noting that CMAS is continuously blown away and redeposited on the blade surface in an actual service environment. Herein, CMAS was recoated every 10 cycles to replenish the amount of CMAS over time. Coating failure is defined when the spallation area of the coating reaches 10% of the entire area.
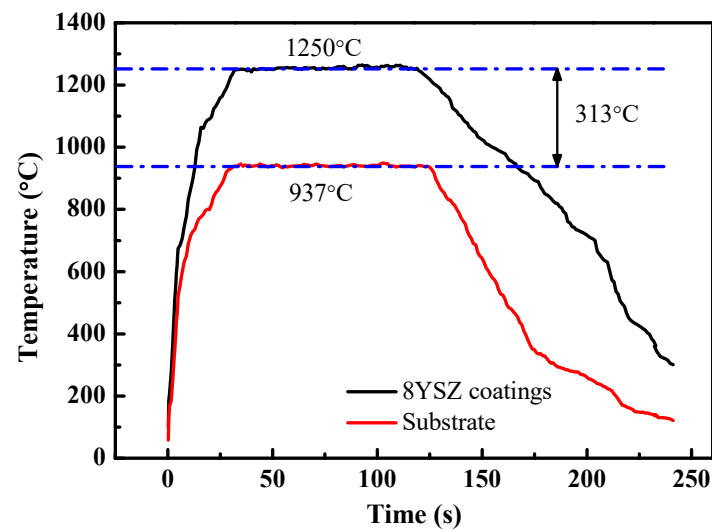
Figure 3. Single thermal shock cycle used for the TBCs.

Table 5. Experimental parameters of environmental simulator test system.

Oxygen Inlet Pressure	Oxygen Inlet Flow	Kerosene Outlet Pressure	Kerosene Flow	Air Pressure	Cooling Gas Inlet Flow
1.5 MPa	180 L/min	0.6 MPa	5 L/h	0.7~0.79 MPa	40 L/min

2.4. Failure Characterization

The phase composition of the ceramic coating after thermal shock failure was determined using X-ray diffraction (XRD, CuKα, Ultimate IV, RIGAKU, Tokyo, Japan). The

scanning range and scanning speed were 10~90° and 0.02°/s, respectively. The surface and cross-section morphologies were obtained using a scanning electron microscope (SEM, TESCAN MIRA3, Brno, Czech Republic). The corresponding element distribution of the coating after failure was detected using an energy spectrometer (EDS, Oxford X MAX20, Oxford, UK). Based on the above methods, the failure mechanism of TBCs under the synergistic effect of thermal shock and CMAS corrosion was analyzed.

3. Results and Discussion

3.1. Phase Structure of 8YSZ Ceramic Coating

XRD patterns of the TBC surface of the as-sprayed specimen and coating after failure are shown in Figure 4. The characteristic peak of the as-sprayed specimen surface is a typical structure of a t-ZrO_2 phase, and there is no occurrence of an impure phase. After the thermal shock cycles, the surface of coating failure had m-ZrO_2 phase peaks in addition to the t-ZrO_2 phase. This suggests that CMAS melts and penetrates the ceramic coating along the EB-PVD columnar structure during the thermal shock process. Meanwhile, CMAS reacted with 8YSZ, and the yttrium element in the coating dissolved in the CMAS, leading to the phase transition of ZrO_2 from the tetragonal phase to the monoclinic phase [12,30]. Moreover, the spinel ($MgAl_2O_4$) and anorthite ($CaAl_2Si_2O_8$) phases were detected on the coating surface due to the reactions between the CMAS paste and the top ceramic coating at high temperatures (1250 °C), as shown in Figure 4b.
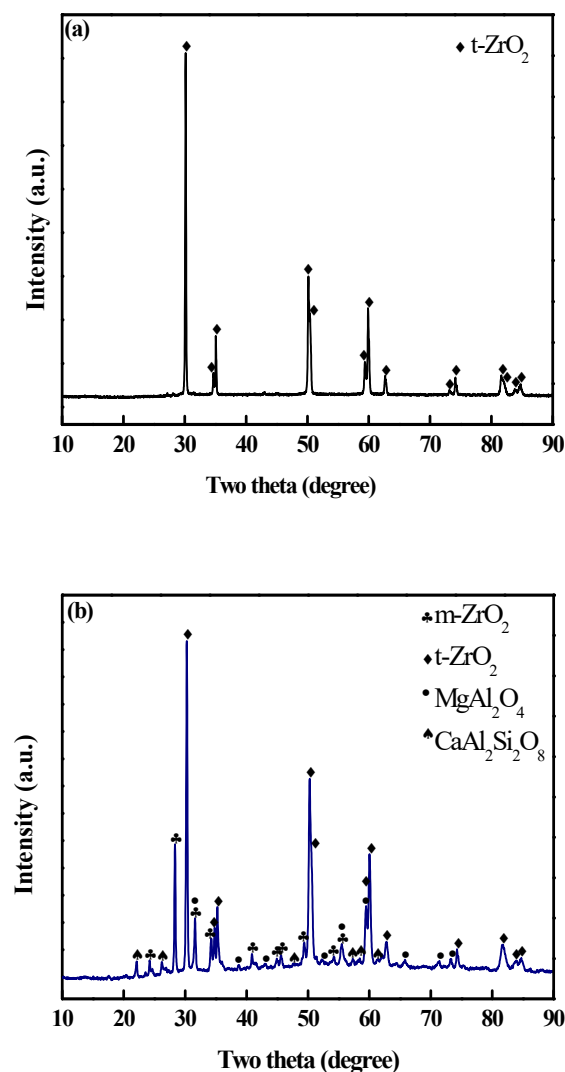

Figure 4. XRD patterns of the TBC surface: (**a**) as-sprayed specimen; (**b**) specimen after failure.

### 3.2. Macro-Morphology and Infrared Thermography Characteristics of TBCs

Figure 5 shows the macro-morphology of three specimens after thermal shock cycles. Some light gray-green spots can be seen on the TBC surface; they are traces of CMAS corrosion. As the number of thermal shock cycles increased, the number of CMAS spots was reduced and the color was lighter. This implies that the molten CMAS penetrated the ceramic coating under the interaction of high temperature and the impact force of a high-speed flame. At the same time, the ceramic coating started to spall from the substrate, and the spallation region continued to expand. The depletion of yttrium accelerated the phase transformation, which caused a 3%~5% volume expansion [16]. Meanwhile, CMAS reacted with 8YSZ, resulting in the performance degradation of the ceramic coating. This, combined with the action of the cold–hot alternating cycle initiated and propagated cracks in the ceramic coating, leading to coating spallation. Figure 6 shows the evolution of infrared thermal images with thermal shock cycles during the holding stage. The temperature distribution was relatively uniform at first. As the number of thermal shock cycle increased, some abnormal temperature regions occurred on the TBC's surface. When compared with the macro-morphology in Figure 5, the abnormal temperature regions correspond to the spallation areas. The abnormal temperature regions increased with an increase in the number of thermal shock cycles.
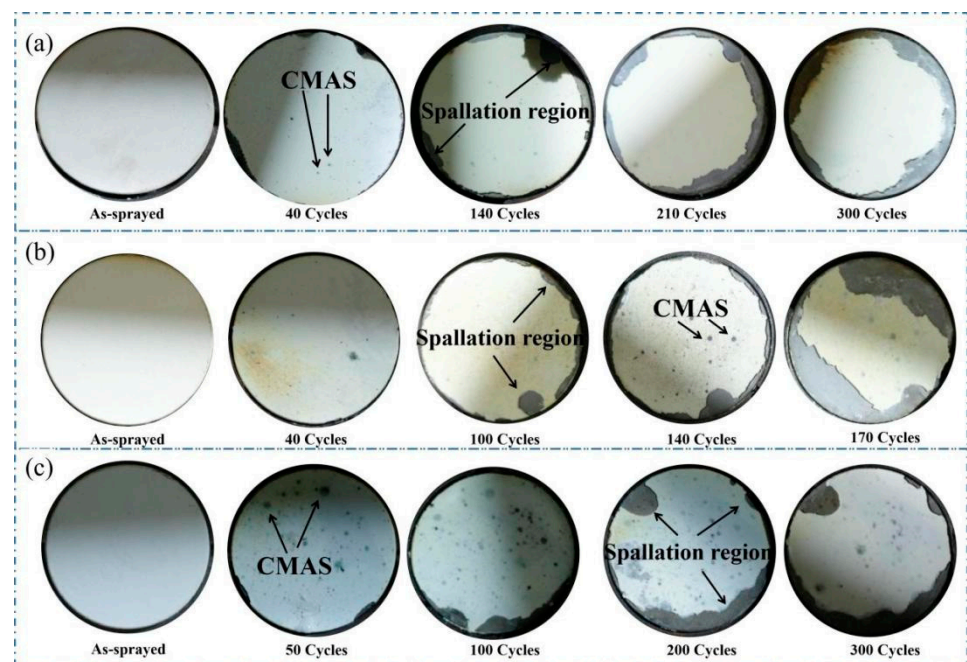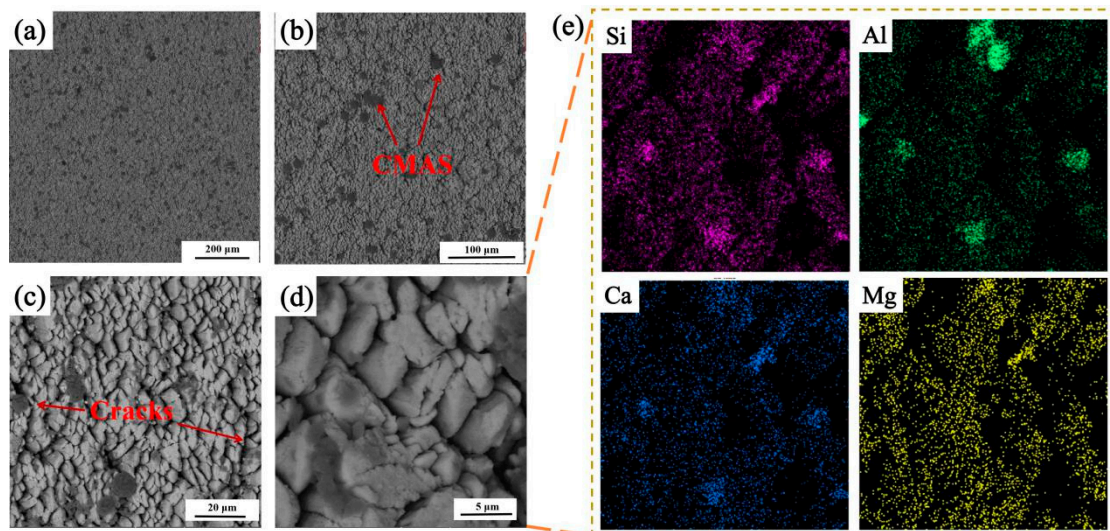

Figure 5. Macro-morphology of the surface of TBCs after thermal shock cycles: (**a**) specimen 1; (**b**) specimen 2; and (**c**) specimen 3.

3.3. Microstructure Characterization

SEM images of the TBC surface and the element distribution of the residual coating after failure are shown in Figure 7. As shown, the coating surface of the columnar structure is covered with dark gray CMAS spots. In the thermal shock cycle process, CMAS melted and filled the columnar gap of the ceramic coating. The top ceramic layer became denser, reducing the strain tolerance of the coating. Figure 7e shows the surface element distribution of Figure 7d. There was an enriched mixture of Ca, Mg, Al, and Si attached to the surface. Molten CMAS slowly penetrated along the columnar gaps at a high temperature. The yttrium element then dissolved in the CMAS, resulting in the phase transition of ZrO_2. The volume expansion induced by phase transition generated tensile stress, which caused coating spallation.
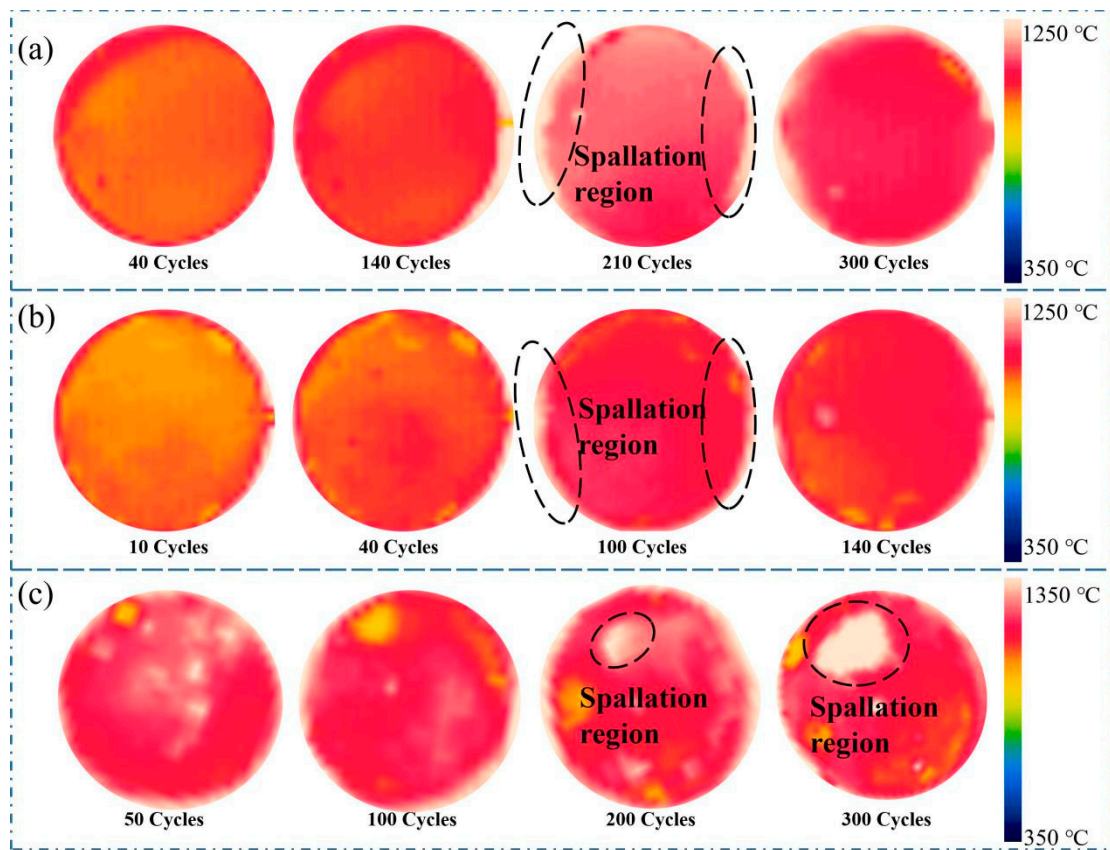
Figure 6. Evolution of infrared thermal images with thermal shock cycles during the holding stage: (**a**) specimen 1; (**b**) specimen 2; and (**c**) specimen 3.


Figure 7. SEM images of the surface of the 8YSZ coating after failure: (**a**–**d**) micro-morphology of the coating surface of sample 1 under different magnifications; (**e**) EDS mapping of the image (**d**).

Cross-sectional SEM images of the TBC specimen after failure are shown in Figure 8. As shown in the completely exfoliated area A, the ceramic coating was delaminated from the interface between the ceramic coating and the TGO. In the partially exfoliated area (area B), surface vertical cracks and interfacial cracks occurred in the ceramic coating. As multiple surface vertical cracks propagated to the interface and merged with interfacial cracks, the ceramic coating spalled from the substrate. Even in an intact area (area C),

surface vertical cracks and horizontal cracks were found in the ceramic coating. A similar experimental phenomenon was obtained by Mercer et al. [31] Due to CMAS infiltration and the chemical reaction between CMAS and 8YSZ, the columnar morphology of the top ceramic layer disappeared. In one sample, due to the loss of the yttrium element, the volume expansion induced by the phase transition of ZrO_2 produced tensile stress, which led to fatal horizontal cracks in the coating. In another, the molten CMAS penetrated the coating and filled the columnar gap, which caused a reduction in the columnar gap. The top ceramic layer became denser, and the strain tolerance of the coating reduced. This structural degradation led to an increase in the elastic modulus and thermal conductivity, which further drove the generation of horizontal cracks [32,33].
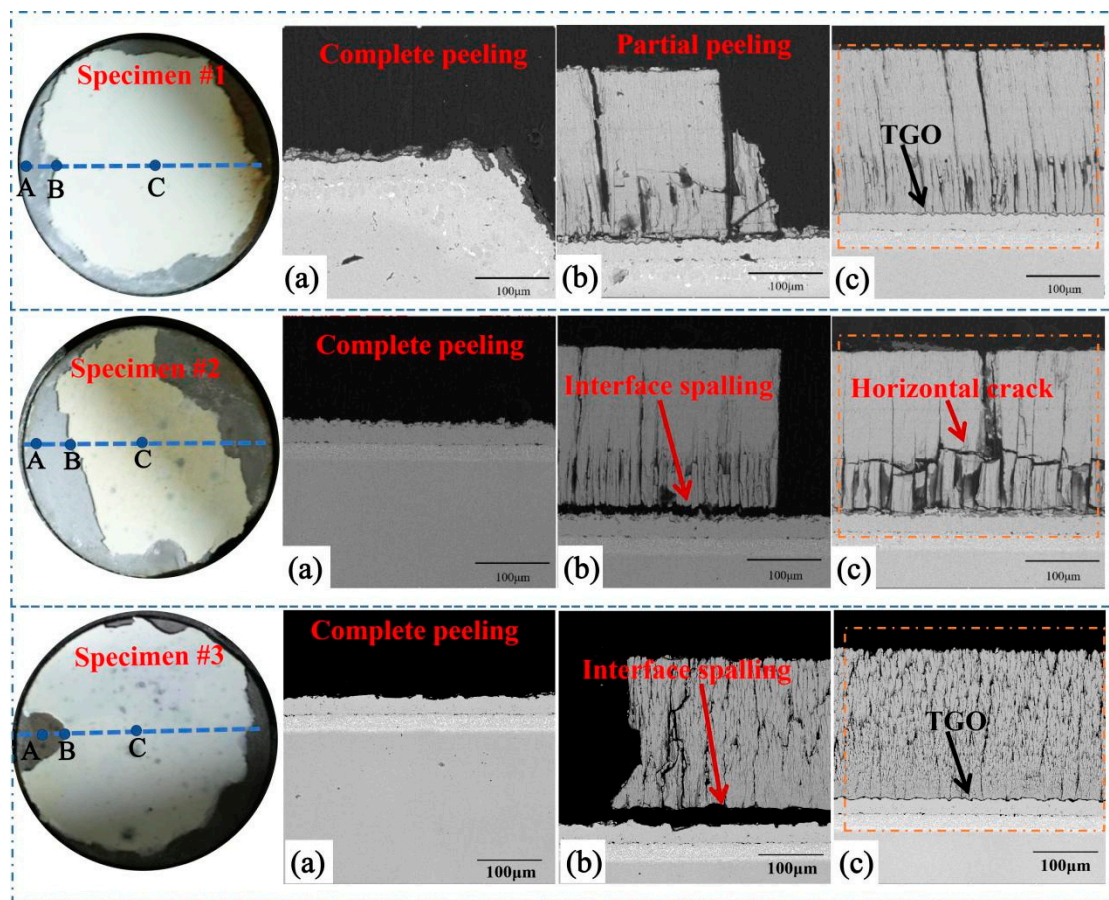
Figure 8. Cross-sectional SEM images of three TBC specimens after failure: (**a**–**c**) cross-sectional morphologies of areas A–C, respectively. Areas A, B, and C represent the complete peeling area, peeling edge area, non-peeling area, respectively. The corresponding microstructures are shown in (**a**–**c**).

Figure 9 shows the cross-sectional EDS results of region C. Because the content of Ca and Si in CMAS is relatively high, the distribution levels of Ca and Si elements are used to determine CMAS infiltration depth. The EDS mappings in Figure 9 show that the Ca and Si elements completely infiltrated the interface between the top coating and the bond coat, indicating that the coating was completely infiltrated by CMAS. Careful point EDS measurements at higher magnifications and at different thickness points within the inter-columnar gaps of TBCs are shown Table 6, and they further confirm that Ca, Mg, Al and Si elements penetrated the entire cross-section of the ceramic coating. Because CMAS was supplied every ten thermal shock cycles, the CMAS concentration near the top ceramic layer was higher than that of other positions. CMAS' attack on the TBC surface was more serious, resulting in severe structural degradation. Combined with the cold–hot

alternating cycle in thermal shock, the out-of-plane tensile stress and in-plane shear stress occurred at the interface between the infiltration and no-infiltration regions; this led to cracks initiating in the coating and coating spallation. This phenomenon is consistent with the result reported by Zhang et al. [34]. Furthermore, a numerical model considering CMAS infiltration, phase transformation and thermal expansion has proven that CMAS infiltration induces significant out-of-plane tensile stress in the ceramic coating, which results in vertical cracks. Phase transformation leads to a further increase in out-of-plane tensile stress and in-plane shear stress, accelerating the coating failure [35].
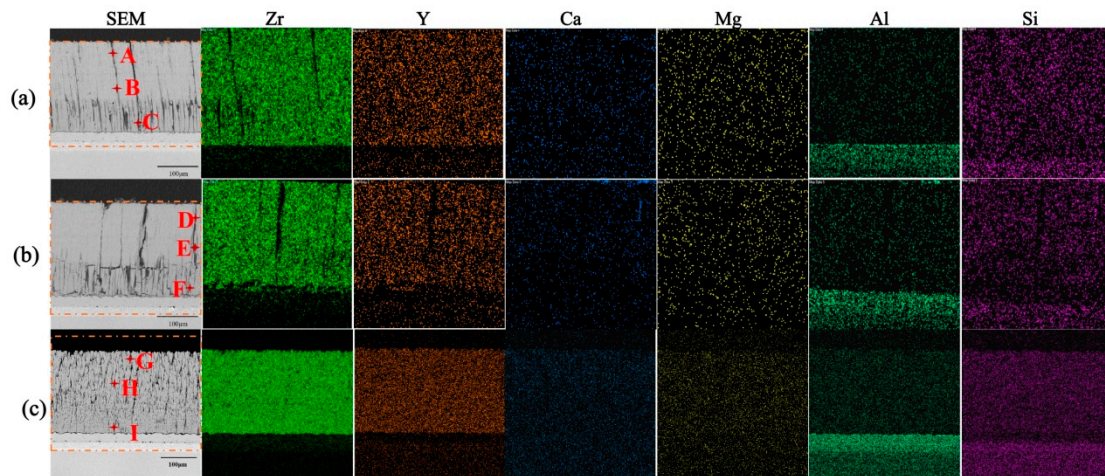
Figure 9. Cross-sectional EDS mapping of the residual coating after failure: (**a**) specimen 1; (**b**) specimen 2; and (**c**) specimen 3. Points A–C, D–F, G–I are the different thickness points within 8YSZ coating of the three specimens, and the corresponding EDS results are shown in Table 6.

Table 6. Chemical compositions of the marked regions in Figure 9.

Location	Composition (at.%)			
	Ca	Mg	Al	Si
A	41.60	6.88	17.36	34.16
B	37.71	7.80	19.80	34.69
C	24.53	4.25	13.82	57.40
D	42.56	7.53	12.87	37.04
E	41.48	6.12	13.48	38.92
F	31.18	4.52	10.79	53.51
G	45.89	6.94	8.54	38.63
H	42.32	5.61	10.05	42.02
I	29.23	5.02	9.67	56.08

4. Conclusions

An 8YSZ ceramic coating was deposited on a PtAl bond coating/DD419 nickel-based single crystal superalloy substrate using the EB-PVD method. The thermo-chemo-mechanical coupling effect of TBCs was studied in a self-developed environmental simulator. The failure mechanism of TBCs under the synergistic effect of thermal shock and CMAS corrosion was investigated using infrared thermography, XRD, SEM and EDS. The main conclusions include:

(1) The temperature distribution and failure process of TBCs were detected in real time using infrared thermography. Combining the infrared thermal images with macro-morphology, it could be observed that the abnormal temperature regions correspond to the damage and spallation position.

(2) CMAS reacted with 8YSZ, and the yttrium element in the coating dissolved in the CMAS, leading to the phase transition of ZrO_2 from the tetragonal phase to the monoclinic

phase. Meanwhile, CMAS filled the columnar gap of the ceramic coating, which caused structural degradation and the disappearance of columnar morphology. The top ceramic layer became denser, and the strain tolerance of the coating reduced.

(3) The failure mechanism of TBCs is that the interaction of volume expansion induced by the phase transition of ZrO_2, structural degradation and thermal fatigue further increases the out-of-plane tensile stress and in-plane shear stress in the ceramic coating. This accelerates the initiation and propagation of surface vertical cracks and horizontal cracks. As multiple surface vertical cracks propagate to the interface and merge with interfacial cracks, the ceramic coating spalls from the substrate.

Institutional Review Board Statement: Not applicable.

Informed Consent Statement: Not applicable.

Data Availability Statement: The raw/processed data required to reproduce these findings cannot be shared at this time as the data also form part of an ongoing study.

Conflicts of Interest: The authors declare that they have no known competing financial interests.

References

1. Vackel, A.; Dwivedi, G.; Sampath, S. Structurally integrated, damage-tolerant, thermal spray coatings. *JOM* **2015**, *67*, 1540–1553. [CrossRef]
2. Mauget, F.; Hamon, F.; Morisset, M.; Cormier, J.; Riallant, F.; Mendez, J. Damage mechanisms in an EB-PVD thermal barrier coating system during TMF and TGMF testing conditions under combustion environment. *Int. J. Fatigue* **2017**, *99*, 225–234. [CrossRef]
3. Guo, H.B.; Gong, S.K.; XU, H.B. Progress in thermal barrier coatings for advanced aeroengines. *Mater. China* **2009**, *28*, 18–26.
4. Miller, R.A. Thermal barrier coatings for aircraft engines: History and directions. *J. Therm. Spray Technol.* **1997**, *6*, 35–42. [CrossRef]
5. Padture, P.N. Thermal barrier coatings for gas-turbine engine applications. *Science* **2002**, *296*, 280–284. [CrossRef]
6. Zhang, D.; Gong, S.; Xu, H.; Wu, Z. Effect of bond coat surface roughness on the thermal cyclic behavior of thermal barrier coatings. *Surf. Coatings Technol.* **2006**, *201*, 649–653. [CrossRef]
7. Shen, Z.; He, L.; Xu, Z.; Mu, R.; Huang, G. LZC/YSZ DCL TBCs by EB-PVD: Microstructure, low thermal conductivity and high thermal cycling life. *J. Eur. Ceram. Soc.* **2019**, *39*, 1443–1450. [CrossRef]
8. Shen, Z.Y.; Liu, Z.; Mu, R.D.; He, L.M.; Liu, G.X. LaGdZrO/8YSZ thermal barrier coatings by EB-PVD: Microstructure, thermal properties and failure mechanism. *Chem. Eng. J. Adv.* **2021**, *5*, 100073. [CrossRef]
9. Levi, C.G.; Hutchinson, J.W.; Vidal-Sétif, M.-H.; Johnson, C.A. Environmental degradation of thermal-barrier coatings by molten deposits. *MRS Bull.* **2012**, *37*, 932–941. [CrossRef]
10. Perepezko, J.H. The hotter the engine, the better. *Science* **2009**, *326*, 1068–1069. [CrossRef]
11. Nieto, A.; Agrawal, R.; Bravo, L.; Hofmeister-Mock, C.; Pepi, M.; Ghoshal, A. Calcia–magnesia–alumina–silicate (CMAS) attack mechanisms and roadmap towards Sandphobic thermal and environmental barrier coatings. *Int. Mater. Rev.* **2021**, *66*, 451–492. [CrossRef]
12. Li, L.; Hitchman, N.; Knapp, J. Failure of Thermal Barrier Coatings Subjected to CMAS Attack. *J. Therm. Spray Technol.* **2009**, *19*, 148–155. [CrossRef]
13. Sohn, Y.H.; Kim, J.H.; Jordan, E.H.; Gell, M. Thermal cycling of EB-PVD/MCrAlY thermal barrier coatings: I. Microstructural development and spallation mechanisms. *Surf. Coat. Technol.* **2001**, *146*, 70–78. [CrossRef]
14. Xu, Z.; Wang, Z.; Huang, G.; Mu, R.; He, L. Morphology, bond strength and thermal cycling behavior of (Ni, Pt)Al/YSZ EB-PVD thermal barrier coatings. *J. Alloys Compd.* **2015**, *651*, 445–453. [CrossRef]
15. Cai, C.; Chang, S.; Zhou, Y.; Yang, L.; Zhou, G.; Wang, Y. Microstructure characteristics of EB-PVD YSZ thermal barrier coatings corroded by molten volcanic ash. *Surf. Coat. Technol.* **2016**, *286*, 49–56. [CrossRef]

16. Krause, A.R.; Garces, H.F.; Dwivedi, G.; Ortiz, A.L.; Sampath, S.; Padture, N.P. Calcia-magnesia-alumino-silicate (CMAS)-induced degradation and failure of air plasma sprayed yttria-stabilized zirconia thermal barrier coatings. *Acta Mater.* **2016**, *105*, 355–366. [CrossRef]

17. Yang, W.; Ye, F. The mechanical and thermal properties, CMAS corrosion resistance, and the wettability of novel thermal barrier material GdTaO4. *Ceram. Int.* **2021**, *47*, 28685–28697. [CrossRef]

18. Mechnich, P.; Braue, W. Solid-State CMAS Corrosion of an EB-PVD YSZ Coated Turbine Blade: Zr^{4+} Partitioning and Phase Evolution. *J. Am. Ceram. Soc.* **2014**, *98*, 296–302. [CrossRef]

19. Mechnich, P.; Braue, W.; Schulz, U. High-Temperature Corrosion of EB-PVD Yttria Partially Stabilized Zirconia Thermal Barrier Coatings with an Artificial Volcanic Ash Overlay. *J. Am. Ceram. Soc.* **2010**, *94*, 925–931. [CrossRef]

20. Drexler, J.M.; Aygun, A.; Li, D.; Vaßen, R.; Steinke, T.; Padture, N. Thermal-gradient testing of thermal barrier coatings under simultaneous attack by molten glassy deposits and its mitigation. *Surf. Coat. Technol.* **2010**, *204*, 2683–2688. [CrossRef]

21. Zhu, W.; Li, Z.Y.; Yang, L.; Zhou, Y.C.; Wei, J.F. Real-time Detection of CMAS Corrosion Failure in APS Thermal Barrier Coatings Under Thermal Shock. *Exp. Mech.* **2020**, *60*, 775–785. [CrossRef]

22. Cao, Y.P.; Ning, X.J.; Wang, Q.S. Thermal shock behavior of Ba(Mg1/3Ta2/3)O3-8YSZ double-ceramic-layer thermal barrier coatings prepared by atmospheric plasma spraying. *Surf. Coat. Technol.* **2021**, *409*, 126842. [CrossRef]

23. Gok, M.G.; Goller, G. Microstructural characterization of GZ/C8YSZ thermal barrier coatings after thermal shock and CMAS+hot corrosion test. *J. Eur. Ceram. Soc.* **2017**, *37*, 2501–2508. [CrossRef]

24. Kirbiyik, F.; Gok, M.G.; Goller, G. Application of thermal gradient and thermal cycling tests to Al2O3/CYSZ functionally graded TBC in the presence of simultaneous hot corrosion and CMAS effects. *Surf. Coat. Technol.* **2022**, *444*, 128688. [CrossRef]

25. Jackson, R.W.; Zaleski, E.M.; Poerschke, D.; Hazel, B.T.; Begley, M.R.; Levi, C.G. Interaction of molten silicates with thermal barrier coatings under temperature gradients. *Acta Mater.* **2015**, *89*, 396–407. [CrossRef]

26. Mack, D.E.; Wobst, T.; Jarligo, M.O.D.; Sebold, D.; Vaßen, R. Lifetime and failure modes of plasma sprayed thermal barrier coatings in thermal gradient rig tests with simultaneous CMAS injection. *Surf. Coat. Technol.* **2017**, *324*, 36–47. [CrossRef]

27. Li, S.; Xu, M.; Zhang, C.; Niu, Y.; Bao, Z.; Zhu, S.; Wang, F. Co-doping effect of Hf and Y on improving cyclic oxidation behavior of (Ni,Pt)Al coating at 1150 °C. *Corros. Sci.* **2020**, *178*, 109093. [CrossRef]

28. Zhu, W.; Zhang, C.; Yang, L.; Zhou, Y.; Liu, Z. Real-time detection of damage evolution and fracture of EB-PVD thermal barrier coatings under thermal shock: An acoustic emission combined with digital image correlation method. *Surf. Coat. Technol.* **2020**, *399*, 126151. [CrossRef]

29. Höser, D.; Wallimann, R.; Von Rohr, P.R. Uncertainty Analysis for Emissivity Measurement at Elevated Temperatures with an Infrared Camera. *Int. J. Thermophys.* **2016**, *37*, 14. [CrossRef]

30. Craig, M.; Ndamka, N.; Wellman, R.; Nicholls, J. CMAS degradation of EB-PVD TBCs: The effect of basicity. *Surf. Coat. Technol.* **2015**, *270*, 145–153. [CrossRef]

31. Mercer, C.; Faulhaber, S.; Evans, A.; Darolia, R. A delamination mechanism for thermal barrier coatings subject to calcium–magnesium–alumino-silicate (CMAS) infiltration. *Acta Mater.* **2005**, *53*, 1029–1039. [CrossRef]

32. Kakuda, T.R.; Levi, C.G.; Bennett, T.D. The thermal behavior of CMAS-infiltrated thermal barrier coatings. *Surf. Coat. Technol.* **2015**, *272*, 350–356. [CrossRef]

33. Evans, A.; Hutchinson, J. The mechanics of coating delamination in thermal gradients. *Surf. Coat. Technol.* **2007**, *201*, 7905–7916. [CrossRef]

34. Zhang, G.; Fan, X.; Xu, R.; Su, L.; Wang, T. Transient thermal stress due to the penetration of calcium-magnesium-alumino-silicate in EB-PVD thermal barrier coating system. *Ceram. Int.* **2018**, *44*, 12655–12663. [CrossRef]

35. Liu, Z.; Yang, L.; Zhou, Q.; Zhou, Y.; Yan, G. Modeling stress evolution in porous ceramics subjected to molten silicate infiltration and corrosion. *Corros. Sci.* **2021**, *191*, 109698. [CrossRef]